Dynamical simulation of bound antiproton-nuclear systems and observable signals of cold nuclear compression

A. B. Larionov,[1,2] I. N. Mishustin,[1,2] L. M. Satarov,[1,2] and W. Greiner[1]
[1]*Frankfurt Institute for Advanced Studies, J. W. Goethe-Universität, D-60438 Frankfurt am Main, Germany*
[2]*Russian Research Center Kurchatov Institute, RU-123182 Moscow, Russia*
(Received 18 February 2008; published 16 July 2008)

On the basis of the kinetic equation with self-consistent relativistic mean fields acting on baryons and antibaryons, we study dynamical response of the nucleus to an antiproton implanted in its interior. By solving numerically the time-dependent Vlasov equation, we show that the compressed state is formed on a rather short time scale of about 4–10 fm/c. This justifies the assumption, that the antiproton annihilation may happen in the compressed nuclear environment. The evolution of the nucleus after antiproton annihilation is described by the same kinetic equation including collision terms. We show, that nucleon kinetic energy spectra and the total invariant mass distributions of produced mesons are quite sensitive observables to the antiproton annihilation in the compressed nucleus.

DOI: 10.1103/PhysRevC.78.014604 PACS number(s): 25.43.+t, 21.30.Fe, 24.10.Jv, 24.10.Lx

I. INTRODUCTION

As has been shown recently in Refs. [1,2], an antiproton implanted in a heavy nucleus serves as an attractor for surrounding nucleons that can lead to a sizable increase of the central nucleon density. This effect is caused by the strong attractive scalar and vector potentials acting on the antiproton, as follows from the G-parity transformation of nuclear potentials [3]. Correspondingly, the antiproton also creates an attractive potential acting on nucleons. This leads to the concentration of nucleons around the antiproton and, as result, to a considerable increase of the nucleon density.

Within the relativistic mean field (RMF) model, the G-parity transformed nuclear optical potential is about -700 MeV at the normal nuclear matter density $\rho_0 = 0.148$ fm^{-3}, while a phenomenological value of an antiproton optical potential is limited within the range of $-(100–350)$ MeV [4–8]. Therefore, in order to fit the empirical optical potential, the antiproton coupling constants with σ-, ω-, and ρ-meson fields should be reduced with respect to the values given by the G-parity transformation. The RMF calculations with reduced coupling constants [2] still show quite strong compressional effects for light and medium nuclei.

An important question, which arises here, is whether the compression process is fast enough to develop before the $\bar{p}$-annihilation. The total $\bar{p}p$-annihilation cross section in vacuum can be parameterized at low relative velocities $v_{\rm rel}$ as

$$\sigma_{\rm ann}^{\bar{p}p} = C + \frac{D}{v_{\rm rel}}, \tag{1}$$

where $C = 38$ mb and $D = 35$ mb $\cdot\, c$ [9]. Using these numbers we can estimate the life time of an antiproton inside the nuclear matter at normal density:

$$\tau_{\rm ann} \simeq \frac{1}{\rho_0 \sigma_{\rm ann}^{\bar{p}p}\, v_{\rm rel}} \simeq 2\ {\rm fm}/c. \tag{2}$$

This is, of course, a very short time in nuclear scale. However, as argued in Ref. [2], this time can become much longer, up to 20 fm/c, for deeply bound antiprotons due to the phase space suppression factors. Therefore, the compression effects can, in-principle, show up in $\bar{p}$-nuclear interactions.

In the present work, we apply a dynamical transport model in order to study the formation and decay of the compressed $\bar{p}$-nuclear system. Our calculations are based on the Giessen Boltzmann-Uehling-Uhlenbeck (GiBUU) model [10], which has been recently supplemented by the relativistic mean fields [11]. Apart from collision terms, the GiBUU model solves the coupled (through the mean fields) Vlasov equations for nucleon and antiproton phase space distribution functions. As is well known [12], the Vlasov equation provides a semiclassical limit of the time-dependent Hartree-Fock calculations. Thus, the compressional effects found in Refs. [1,2] should also be reproduced as a static solution of the coupled Vlasov equations.

It will be demonstrated that the compression process is characterized by the time scale which is comparable with the $\bar{p}$ life time in nuclear environment. Thus, $\bar{p}$ has, indeed, a chance to annihilate inside the compressed nucleus. We will show, that the $\bar{p}$-annihilation in a compressed nucleus should lead to the collective expansion of the residual nuclear system. The appearance of the high-energy tails in the kinetic energy spectra of the emitted nucleons is predicted. The distributions in the total invariant mass of produced mesons reveal a noticeable shift toward lower invariant masses, when the annihilation takes place inside the compressed nucleus.

The annihilation of slow antiprotons inside heavy nuclei was, first, proposed by Rafelski [13] as a unique opportunity to study nuclear matter in unusual conditions. Later, Cahay *et al.* [14] studied the $\bar{p}$ annihilation inside nuclei within an intranuclear cascade model. In Ref. [14], antiproton annihilation events into pions at the center of ^{40}Ca and ^{108}Ag nuclei were simulated. The mean field effects were, however, completely neglected in [14].

In Sec. II, we describe the theoretical model applied in calculations. Section III contains the results of the time evolution study for the compression and explosion dynamics. In Sec. IV, we propose several observable signals sensitive to

the $\bar{p}$-annihilation in the compressed nucleus. The summary and outlook are given in Sec. V.

II. THE MODEL

In calculations, we apply the GiBUU model developed in Giessen University. For the detailed description and related references, we refer the reader to the webpage [10], where the new version of the model is presented. Below, we mostly describe the new features implemented in the present work.

A. Relativistic mean fields

Below we consider a system composed of an antinucleon interacting with baryons. This system is described by the RMF Lagrangian of the following form [2,15]:

$$\mathcal{L} = \sum_{j=B,\bar{N}} \bar{\psi}_j[\gamma_\mu(i\partial^\mu - g_{\omega j}\omega^\mu) - m_j - g_{\sigma j}\sigma]\psi_j + \frac{1}{2}\partial_\mu\sigma\partial^\mu\sigma - U(\sigma) - \frac{1}{4}F_{\mu\nu}F^{\mu\nu} + \frac{1}{2}m_\omega^2\omega_\mu\omega^\mu, \quad (3)$$

where ψ_j are the baryon ($j = B \equiv N, N^\star, \Delta, Y$) and antinucleon ($j = \bar{N}$) fields, respectively; σ is the isoscalar-scalar meson field ($I^G = 0^+$, $J^\pi = 0^+$); ω^μ is the isoscalar-vector meson field ($I^G = 0^-$, $J^\pi = 1^-$); and $F_{\mu\nu} \equiv \partial_\mu\omega_\nu - \partial_\nu\omega_\mu$. Here $N^\star$ and Δ denotes, respectively, the isospin 1/2 and 3/2 nonstrange baryonic resonances, and Y stands for the $S = -1$ baryons explicitly propagated in the GiBUU model [10]. In the case of the spin 3/2, 5/2 and 7/2 baryonic resonances, their fields ψ_j carry also one or more vector indices, which are dropped in Eq. (3) and below for brevity. When appropriate, the covariant summation is assumed over these indices. For simplicity, the isovector and electromagnetic terms are disregarded in Eq. (3). The self-interactions of the σ-field are included in Eq. (3) via the term $U(\sigma)$ in order to avoid an unrealistically high compressibility coefficient of the nuclear matter [16]:

$$U(\sigma) = \tfrac{1}{2}m_\sigma^2\sigma^2 + \tfrac{1}{3}g_2\sigma^3 + \tfrac{1}{4}g_3\sigma^4. \quad (4)$$

Some comments are in order to gain more insight into Eq. (3). Following Ref. [2], the antinucleon field $\psi_{\bar{N}}$ in the Lagrangian density (3) is represented in terms of wave functions of *physical antinucleons*. These wave functions can be obtained by the G-parity transformation acting on the wave functions of the Dirac sea nucleons (see Ref. [3] for details), which appear in the relativistic description of the nucleon [17]. By applying the same transformation, the nonlinear RMF Lagrangian of Refs. [15,16] (neglecting terms responsible for the baryon-antibaryon annihilation) can be expressed as Eq. (3) with the following relations between coupling constants:

$$g_{\omega\bar{N}} = -g_{\omega N}, \quad g_{\sigma\bar{N}} = g_{\sigma N}. \quad (5)$$

The relations (5) are satisfied if the physical system would be exactly symmetric with respect to the G-parity transformation. However, this is not necessary to be true in a many-body system [2,3]. The reason is that the concept of the G-parity symmetry is strictly applicable on the level of the elementary processes only. However, the RMF Lagrangian (3) is dealing with the effective interactions, which are usually tuned to describe the bulk properties of the nuclear medium and/or the properties of some selected nuclei. Due to the many-body effects, such as the Pauli blocking or mixed scalar-vector terms in the scattering amplitudes, these effective interactions may not obey the exact G-parity symmetry anymore. To take into account possible deviations from the G-parity symmetry, we introduce an overall scaling of the antinucleon-meson coupling constants with respect to the values given by Eq. (5) (see Ref. [2]):

$$g_{\omega\bar{N}} = -\xi g_{\omega N}, \quad g_{\sigma\bar{N}} = \xi g_{\sigma N}, \quad (6)$$

where $0 < \xi \leqslant 1$ is a scaling factor.

Throughout the paper, we consider two options for the scaling factor of the antinucleon-meson coupling constants: $\xi = 1$, motivated by the G-parity, and $\xi = 0.3$, which is in a better agreement with the empirical $\bar{p}$A optical potential. For other baryonic fields we put in the present work, for simplicity, the same coupling constants as for the nucleon: $g_{\omega N^*} = g_{\omega\Delta} = g_{\omega Y} = g_{\omega N}$, $g_{\sigma N^*} = g_{\sigma\Delta} = g_{\sigma Y} = g_{\sigma N}$.

All calculations have been performed emloying the NL3 parametrization [15] of the RMF model. This parametrization provides quite reasonable nuclear matter properties: the binding energy 16.299 MeV/nucleon, the compressibility coefficient $K = 271.76$ MeV and the nucleon effective mass $m_N^* = 0.60m_N$ at ρ_0. Moreover, the NL3 parametrization reproduces the ground state properties of spherical and deformed nuclei very well [15].

The Dirac equations of motion for baryons have the following form:

$$(\gamma^\mu(i\partial_\mu - g_{\omega j}\omega_\mu) - m_j^\star)\psi_j = 0, \quad (7)$$

where

$$m_j^\star = m_j + g_{\sigma j}\sigma \quad (8)$$

is the effective (Dirac) mass.

Within the mean field approximation the σ- and ω-fields are treated classically. They satisfy the (nonlinear) Klein-Gordon–like equations with the source terms due to coupling to baryons and an antinucleon:

$$\partial_\nu\partial^\nu\sigma + \frac{\partial U(\sigma)}{\partial\sigma} = -\sum_{j=B,\bar{N}} g_{\sigma j}\rho_{Sj}, \quad (9)$$

$$\left(\partial_\nu\partial^\nu + m_\omega^2\right)\omega^\mu = \sum_{j=B,\bar{N}} g_{\omega j}\, j_{bj}^\mu, \quad (10)$$

where $\rho_{Sj} = \langle\bar{\psi}_j\psi_j\rangle$ is the partial scalar density and $j_{bj}^\mu = \langle\bar{\psi}_j\gamma^\mu\psi_j\rangle$ is the partial baryon current. Equation (10) has to be supplemented by the four-transversality condition

$$\partial_\mu\omega^\mu = 0. \quad (11)$$

B. Covariant kinetic equations

Instead of solving the Dirac equations (7), we will describe the baryons and antinucleon dynamics by the coupled set of

the semiclassical kinetic equations [11,18–21]:

$$\frac{1}{p_0^\star}\left[p^{\star\mu}\frac{\partial}{\partial x^\mu}+\left(g_{\omega j}p^\star_\mu F^{k\mu}+m_j^\star\frac{\partial m_j^\star}{\partial x_k}\right)\frac{\partial}{\partial p^{\star k}}\right]f_j(x,\mathbf{p}^\star) = I_j[f_B, f_M], \tag{12}$$

where $k = 1, 2, 3$; $\mu = 0, 1, 2, 3$; $x \equiv (t, \mathbf{r})$; and $f_j(x, \mathbf{p}^\star)$ is the distribution function (DF) in a six-dimensional phase space $(\mathbf{r}, \mathbf{p}^\star)$ with $\mathbf{p}^\star$ being the spatial components of the kinetic four-momentum

$$p^{\star\mu} = p^\mu - g_{\omega j}\omega^\mu. \tag{13}$$

The baryons and antinucleon are assumed to be on the respective effective mass shells:

$$p^{*0} = \sqrt{(\mathbf{p}^\star)^2 + (m_j^\star)^2}. \tag{14}$$

The left hand side (lhs) of Eq. (12) describes the propagation of the jth type particles in the classical σ- and ω-fields. The right hand side (rhs) of Eq. (12) is a collision integral, which represents the (in)elastic two-body collisions with corresponding vacuum cross sections as well as the resonance decays. The complete description of the collision integral structure, in particular, the differential elementary cross sections included into the GiBUU model can be found in [10,11] and in references therein. The in-medium modification of the baryon-baryon and baryon-meson cross sections is neglected in the present work.

We will apply the full kinetic equations, including collision terms, only to describe the *post-annihilation* evolution of a system. By this reason, the antiproton DF is excluded from the collision integral. Instead, we enforce $\bar{p}$ to annihilate into mesons at some preselected time (see Sec. II E). Thus, in the present work the collision integral includes the nucleon, $\Delta(1232)$ and higher baryon resonances up to the mass of 2 GeV, which can be excited in the meson-baryon and baryon-baryon collisions. A possible hyperon formation in the processes $\pi N \to YK$ and $\bar{K}N \to \pi Y$ is included too. The "valence mesons" $M \equiv \pi, \eta, \rho, \sigma, \omega, \eta', \phi, \eta_c, J/\psi, K, \bar{K}, K^*, \bar{K}^*$ are explicitly taken into account. They are assumed to propagate freely between collisions, i.e., we neglect the mean field potentials acting on these mesons.

The scalar density and the baryon current of the jth type baryons are expressed in terms of DF as follows:

$$\rho_{Sj}(x) = \frac{g_j}{(2\pi)^3}\int\frac{d^3p^\star}{p^{\star 0}}m_j^\star f_j(x,\mathbf{p}^\star), \tag{15}$$

$$j^\mu_{bj}(x) = \frac{g_j}{(2\pi)^3}\int\frac{d^3p^\star}{p^{\star 0}}p^{\star\mu} f_j(x,\mathbf{p}^\star), \tag{16}$$

where g_j is the spin-isospin degeneracy factor ($g_N = g_{\bar{N}} = 4$, $g_\Delta = 16$, etc.).

One can show [21,22] that the kinetic equations (12) with the σ- and ω-fields evolving according to Eqs. (9), (10) lead to the continuity equations

$$\sum_{j=B}\partial_\mu j^\mu_{bj} = 0, \quad \partial_\mu j^\mu_{b\bar{N}} = 0 \tag{17}$$

and the energy-momentum conservation

$$\partial_\nu T^{\mu\nu} = 0, \tag{18}$$

where the energy-momentum tensor is written as

$$T^{\mu\nu} = \sum_{j=B,\bar{N},M}\frac{g_j}{(2\pi)^3}\int\frac{d^3p^\star}{p^{\star 0}}p^\mu p^{\star\nu} f_j(x,\mathbf{p}^\star) + \partial^\mu\sigma\partial^\nu\sigma - \partial^\mu\omega^\lambda\partial^\nu\omega_\lambda - g^{\mu\nu}\left(\frac{1}{2}\partial_\lambda\sigma\partial^\lambda\sigma - U(\sigma) - \frac{1}{2}\partial_\lambda\omega_\kappa\partial^\lambda\omega^\kappa + \frac{1}{2}m_\omega^2\omega^2\right). \tag{19}$$

Here we have also included possible contributions of the "valence" mesons M, which can be produced at the annihilation. It is assumed that $p^\star = p$ for the valence mesons.

C. Numerical realization

In order to solve Eq. (12) numerically, DF is represented by the set of point-like test particles:

$$f_j(x,\mathbf{p}^\star) = \frac{(2\pi)^3}{g_j n}\sum_{i=1}^{nN_j}\delta(\mathbf{r}-\mathbf{r}_i(t))\delta(\mathbf{p}^\star-\mathbf{p}_i^\star(t)), \tag{20}$$

where N_j is the number of physical particles of the type j and n is the number of test particles per physical particle (the same for all types j). The test particle positions $\mathbf{r}_i$ and kinetic momenta $\mathbf{p}_i^\star$ are evolving in time according to the following equations:

$$\dot{\mathbf{r}}_i = \frac{\mathbf{p}_i^\star}{p_i^{\star 0}}, \tag{21}$$

$$\dot{p}_i^{\star k} = g_{\omega j}\frac{p^\star_{i\mu}}{p_i^{\star 0}}F^{k\mu} + \frac{m_j^\star}{p_i^{\star 0}}\frac{\partial m_j^\star}{\partial x_k} \tag{22}$$

with $k = 1, 2, 3$ and $\mu = 0, 1, 2, 3$. It is easy to check that DF (20) with $\mathbf{r}_i$ and $\mathbf{p}_i^\star$ satisfying Eqs. (21), (22) gives a formal solution of the Vlasov equation in the case when the collision integral in Eq. (12) is equal to zero. Equations (21), (22) are equivalent to the Hamiltonian equations of motion for the test particle positions $\mathbf{r}_i$ and canonical momenta $\mathbf{p}_i$:

$$\dot{\mathbf{r}}_i = \frac{\partial p_i^0}{\partial \mathbf{p}_i}, \tag{23}$$

$$\dot{\mathbf{p}}_i = -\frac{\partial p_i^0}{\partial \mathbf{r}_i}, \tag{24}$$

where $p_i^0 = g_{\omega j}\omega^0 + \sqrt{(\mathbf{p}_i^\star)^2 + (m_j^\star)^2}$ is the single-particle energy (see [21,23]). However, it is more convenient to propagate in time the test particle kinetic momenta rather than the canonical ones, since then Eq. (9) for the σ-field decouples from Eq. (10) for the ω-field.

When the collision integral in Eq. (12) is taken into account, the test particles are propagated between the two-body collisions using Eqs. (21), (22). All calculations have been performed in the parallel ensemble mode. In this mode, the two-body collisions are permitted between the test particles belonging to the same parallel ensemble only, while the mean field is averaged over n parallel ensembles of the test particles propagated simultaneously [see Eq. (20)]. Therefore, a single parallel ensemble can be considered as a physical event.

In actual calculations, we have neglected the time derivatives of the meson fields in Eqs. (9), (10). However, the spatial derivatives were treated without any simplifying assumptions. The reason for such a strategy is that we are dealing with nuclear systems which have large density gradients, but evolving slowly, as compared with the spatial and temporal scales involved in the mesonic equations of motion. Indeed, including the temporal gradients would lead to the frequent oscillations of the mesonic fields with a period of less than $2\pi/m$, where m is the meson mass. This gives the period of 2.5 fm/c (1.5 fm/c) for the σ-(ω-)field. By taking into account the finite wave lengths of these oscillations would further reduce the periods. The treatment of such oscillations would strongly complicate the numerical calculations, in particular, due to the classical meson field radiation. On the other hand, the characteristic periods of the oscillations are significantly smaller than the characteristic compression times (4–10 fm/c, see Sec. III A below). Therefore, one can approximately average out the mesonic fields with respect to these oscillations, that is actually assumed in our model. The σ- and ω-fields are, therefore, calculated from the equations

$$-\triangle\sigma + \frac{\partial U(\sigma)}{\partial\sigma} = -\sum_{j=B,\bar{N}} g_{\sigma j}\rho_{Sj}, \tag{25}$$

$$\left(-\triangle + m_\omega^2\right)\omega^\mu = \sum_{j=B,\bar{N}} g_{\omega j} j_{bj}^\mu. \tag{26}$$

Within the same approximation, the energy-momentum tensor has the following form:

$$\begin{aligned} T^{\mu\nu} = & \sum_{j=B,\bar{N},M} \frac{g_j}{(2\pi)^3}\int \frac{d^3p^\star}{p^{\star 0}} p^\mu p^{\star\nu} f_j(x,\mathbf{p}^\star) \\ & + (\partial^\mu\sigma\partial^\nu\sigma - \partial^\mu\omega^\lambda\partial^\nu\omega_\lambda)(1-\delta_{\nu 0}) \\ & - g^{\mu\nu}\left(-\frac{1}{2}(\nabla\sigma)^2 - U(\sigma) + \frac{1}{2}\nabla\omega_\lambda\nabla\omega^\lambda + \frac{1}{2}m_\omega^2\omega^2\right). \end{aligned} \tag{27}$$

The factor $(1-\delta_{\nu 0})$ in Eq. (27) reflects the fact, that due to the omission of the time derivatives of the meson fields in the Lagrangian density, only the first term in the rhs contributes to the three-momentum density $T^{\alpha 0}$ ($\alpha = 1, 2, 3$).

Although Eqs. (25), (26) are not covariant, they provide a better description of the nuclear surface than pure local fields [11]. This improves the stability of a nuclear ground state and is more appropriate for studying nuclear response to external hadronic and electromagnetic probes.

Equations (25), (26) have been solved numerically by applying the alternating direction implicit iterative method of Douglas described in Ref. [24]. Due to the scalar density dependence on the effective mass [see Eqs.(8), (15)], additional iterations are needed to solve Eq. (25). In other words, the scalar density has to be computed self-consistently. To evaluate the meson fields, we used a uniform grid in coordinate space with steps $\Delta_x = \Delta_y = \Delta_z$. For the systems $\bar{p}^{16}$O, $\bar{p}^{40}$Ca and $\bar{p}^{208}$Pb considered below, the grid covered a cubic volume with the side of 10, 20, and 30 fm, respectively, centered at the center of mass (c.m.) of a $\bar{p}$A system. By numerical reasons, the δ-functions in coordinate space, introduced in Eq. (20), have been replaced by the Gaussians of the width L:

$$\delta(\mathbf{r}-\mathbf{r}_i(t)) \Rightarrow \frac{1}{(2\pi)^{3/2}L^3}\exp\left\{-\frac{(\mathbf{r}-\mathbf{r}_i(t))^2}{2L^2}\right\}. \tag{28}$$

The width of the Gaussian and the grid step sizes are pure numerical parameters which should resolve the coordinate space nonuniformities of the system. In our case the characteristic space scale is given by the radius of the smallest considered nucleus ^{16}O, i.e., $\simeq 3$ fm. On the other hand, in order to have smooth density distributions, the number n of test particles per physical particle [see Eq. (20)] should be correlated to the width of the Gaussian as $n \propto L^{-3}$. This puts a restriction on too small width due to CPU time increase. As an optimum choice, we fixed in the present work $\Delta_x = \Delta_y = \Delta_z = L = 0.5$ fm. We have realised, however, that there is a rather moderate tendency of increasing maximum compression (see discussion in Sec. III A below) with decreasing Gaussian width. The number of test particles per nucleon was set to $n = 1500$ in the most of calculations.

The equations of motion (21), (22) have been solved by applying the second-order in time predictor-corrector method [11] with the time step of 0.1 fm/c. This value is small enough to resolve the time scale of a few fm/c for the compression processes (see Figs. 3 and 5 below). We have checked, that taking smaller time step does not influence the results. The full numerical scheme conserves the total energy with the accuracy of about 5% of the initial total binding energy of the $\bar{p}A$ system.

D. Initialization

The nucleons were distributed in coordinate space according to the Woods-Saxon density profile. The momenta of nucleons were sampled according to the local Fermi distribution.

The initial antiproton DF was chosen as a Gaussian wave packet in coordinate and momentum space [25,26] located at the center of a nucleus ($x = y = z = 0$):

$$f_{\bar{N}}(t=0,\mathbf{r},\mathbf{p}^\star) = \frac{(2\pi)^3}{g_{\bar{N}}\pi^3}\exp\left\{-\mathbf{r}^2/\left(2\sigma_r^2\right) - 2\sigma_r^2\mathbf{p}^{\star 2}\right\}, \tag{29}$$

where σ_r is the width in coordinate space. Equation (29) implies that the antiproton is at rest. The width of the initial antiproton distribution in momentum space is $(2\sigma_r)^{-1}$, which follows from the uncertainty relation. If not mentioned explicitly, the calculation is done with the choice $\sigma_r = 1$ fm. This value agrees with results of the static RMF calculations of Ref. [2]. As for nucleons, the antiproton DF (29) is projected onto test particles according to Eq. (20) with the δ-functions in coordinate space replaced by Gaussians. To avoid misunderstanding, we note that one should distinguish the width σ_r of the physical antiproton spatial distribution in Eq. (29) and the width of the test particle Gaussian.

E. Propagation and annihilation

After the initialization, the system of nucleons and antiproton was propagated in time according to Eqs. (21), (22). The meson fields have been calculated by Eqs. (25), (26) with

the source terms given by the scalar densities (15) and the baryon currents (16). In such a way, the evolution of the system toward compressed state has been followed. In this calculation, the collision term in the rhs of the kinetic equation (12) has been set to zero, i.e., we considered a pure mean-field Vlasov dynamics. This was done to see most clearly the role of the mean fields. An introduction of the $\bar{N}N$ and NN elastic collisions would mainly lead to a dissipation of the collective energy into heat. As pointed out in Ref. [2], this effect is rather small and, therefore, can not change significantly the compression dynamics.

The reason is that the elastic collisions are not frequent on the time scale of compression (see Figs. 3, 4, and 5 below). Indeed, the mean time $\tau_{\rm coll}$ between nucleon-nucleon collisions can be estimated as $\tau_{\rm coll} = 1/(\rho_N \sigma_{NN} v_F)$, where $\sigma_{NN} \simeq 40$ mb is the elastic nucleon-nucleon cross section (c.f. Refs. [27,28]) and $v_F \simeq 0.3c$ is the Fermi velocity. This gives $\tau_{\rm coll} =$ 3–6 fm/c for the nucleon density $\rho_N = 2$–$1\rho_0$. The Pauli blocking effect will further increase $\tau_{\rm coll}$. A similar estimate can also be done for $\bar{N}N$ elastic collisions.

At certain time moment $t_{\rm ann}$, which is an external parameter to our model, we simulated the annihilation of an antiproton. This implies that annihilation occurs instantaneously, as a single quantum mechanical transition, in distinction to description of this process via the collision term in a kinetic equation. In the last case, the antiproton distribution function would gradually disappear on the way to the compressed state. The purpose of the present work is to look at the strongest possible effect of the nuclear compression on observables. Therefore, we let the compressed system to be formed, and simulate the sudden annihilation afterwards. The ambiguity in the in-medium annihilation cross sections is taken into account by varying the parameter $t_{\rm ann}$.

In the actual calculations, the annihilation was simulated as follows: For each antiproton test particle, the closest in coordinate space nucleon test particle was chosen to be the annihilation partner. At large enough values of the total in-medium c.m. energy $\sqrt{s}$ of the annihilating $\bar{p}N$ pair (see below), the annihilation event of the test particle pair into mesons was simulated using the quark model [29,30], which has been already implemented in the GiBUU model [10] earlier. A quark and an antiquark with the same flavor are assumed to annihilate and transfer their total four-momentum to the remaining (anti)quarks. The remaining four (anti)quarks form two orthogonal $q\bar{q}$ jets with equal energies in the c.m. frame. The jets were hadronized via the Lund string fragmentation model [31] in the JETSET version included into the PYTHIA 6.225 program package. The applied annihilation model corresponds to the R2 type diagram in classification of Ref. [9], i.e., to the quark rearrangement with one $q\bar{q}$ annihilation vertex. In this sense, the model has some similarity with the two-meson doorway models of Refs. [32,33]. To illustrate how the model works we have performed simulations of the $p\bar{p}$ annihilation.

Figure 1 shows the pion multiplicity distribution for the $p\bar{p}$ annihilation at rest in vacuum compared to the data compilation from Refs. [9,34]. The calculated distribution is somewhat shifted to smaller pion multiplicities with respect to the data: The calculated average pion multiplicity $\langle n_\pi \rangle \simeq 4.5$

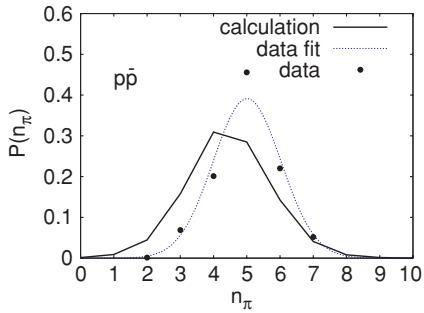

FIG. 1. (Color online) Pion multiplicity distribution for $p\bar{p}$ annihilation at rest in vacuum. Data points are from Ref. [9]. The dashed line represents the data fit [34] with the Gaussian $P(n_\pi) = \exp\{-(n_\pi - < n_\pi >)^2/2\sigma^2_{n_\pi}\}/\sqrt{2\pi\sigma^2_{n_\pi}}$ where $< n_\pi >= 5.01$ and $\sigma^2_{n_\pi} = 1.04$.

compared with the experimental value of $\simeq 5.0$. We would like to remark, that non-vanishing contribution of the $n_\pi = 2$ channel in calculations is completely due to the final states with other particles: $\pi\pi\eta$ (78%), $\pi\pi K\bar{K}$ (14%), $\pi\pi\eta\eta$(6%) and $\pi\pi+$ photons (2% before η decay). In calculations, we took into account η decays into 2γ or into final states with pions and disregarded photons afterwards. However, it is not clear to us how photons were counted in the data (see also Ref. [32]).

Figure 2 shows the calculated charged pion momentum distributions in the c.m. frame of the annihilating $p\bar{p}$ pair at rest in vacuum. From the partial contributions of the channels with various pion multiplicities we observe, as expected, that the hard (soft) part of the total momentum distribution is populated mainly by the low (high) pion multiplicity events. The experimental data are described reasonably well, except for the momenta $0.5 \leqslant k \leqslant 0.7$ GeV/c, where the calculations significantly overestimate the data.

We believe that the accuracy of the model in describing the data in Figs. 1 and 2 is sufficient for the exploratory studies of global observables in the present work. Certainly, the improvement of the annihilation model is needed to

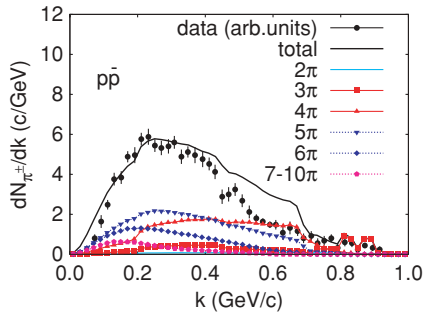

FIG. 2. (Color online) Charged pion momentum distribution for $p\bar{p}$ annihilation at rest in vacuum. The total calculated distribution is shown by the thick solid line. The calculated partial contributions from events with various pion numbers are also depicted (see key for notations). The calculations are normalized to the number of charged pions per annihilation event. Data from Ref. [9] are in arbitrary units and are rescaled to agree with calculations at $k = 0.3$ GeV/c.

perform more detailed study of the mesonic final states in the annihilation. Below we concentrate more on the in-medium effects on the annihilation.

Due to the mean field, the invariant energy of the annihilating $\bar{p}N$ pair can be substantially below the vacuum threshold value of $2m_N$. This makes the direct application of the JETSET model for the $\bar{p}$-annihilation in nuclei physically and numerically problematic. To overcome this difficulty, we introduced the corrected invariant energy as follows [11,35]:

$$\sqrt{s_{\rm corr}} = \sqrt{s^\star} - 2(m_N^\star - m_N), \tag{30}$$

where $s^\star = (p_{\bar{p}}^\star + p_N^\star)^2$. The quantity $\sqrt{s_{\rm corr}}$ is a vacuum analog of the total in-medium invariant c.m. energy $\sqrt{s}$ with $s = (p_{\bar{p}} + p_N)^2$. Provided that $\sqrt{s} > 4m_\pi$, we have used $\sqrt{s_{\rm corr}}$ in the JETSET simulation in order to produce the mesonic final states. This lower limit of $\sqrt{s}$ is due to the fact that the JETSET model does not generate enough direct 2π and 3π annihilation final states.

In order to take into account the in-medium effects, in particular, to ensure the correct in-medium threshold condition $\sqrt{s} > m_1 + m_2 + \cdots + m_{n_{\rm mes}}$, where $m_1, m_2, \ldots, m_{n_{\rm mes}}$ are the vacuum masses of the produced mesons, the annihilation event was accepted with the probability

$$\mathcal{P} = \frac{\Phi_{n_{\rm mes}}(\sqrt{s}; m_1, m_2, \ldots, m_{n_{\rm mes}})}{\Phi_{n_{\rm mes}}(\sqrt{s_{\rm corr}}; m_1, m_2, \ldots, m_{n_{\rm mes}})}, \tag{31}$$

where

$$\Phi_{n_{\rm mes}}(\sqrt{s}; m_1, m_2, \ldots, m_{n_{\rm mes}}) = \int \frac{d^3k_1}{(2\pi)^3 2\omega_1} \int \frac{d^3k_2}{(2\pi)^3 2\omega_2} \cdots \int \frac{d^3k_{n_{\rm mes}}}{(2\pi)^3 2\omega_{n_{\rm mes}}} \times \delta^{(4)}(p_{\bar{p}} + p_N - k_1 - k_2 - \cdots - k_{n_{\rm mes}}) \tag{32}$$

is the invariant phase space volume, $k_i = (\omega_i, \mathbf{k_i})$ are the four-momenta of the produced mesons satisfying the vacuum mass shell conditions $m_i^2 = k_i^2$, $i = 1, 2, \ldots, n_{\rm mes}$. Finally, the three-momenta of the produced mesons in the c.m. frame of the annihilating $\bar{p}N$ pair were multiplied by the common factor adjusted to get the correct in-medium total c.m. energy $\sqrt{s}$.

In fact, the way we simulate the in-medium effects Eq. (31) implies using the vacuum matrix elements of the annihilation channels, which are given by the JETSET model, while taking into account the in-medium effects in the phase space factors only. Similar procedures have been applied earlier in Refs. [2,11,35].

At $2m_\pi < \sqrt{s} \leqslant 4m_\pi$, the final 2π or 3π channel was chosen by Monte Carlo according to the probability ratio

$$\frac{\mathcal{P}_{2\pi}}{\mathcal{P}_{3\pi}} = R_0 \frac{\Phi_2(\sqrt{s}; m_\pi, m_\pi)\Phi_3(2m_N; m_\pi, m_\pi, m_\pi)}{\Phi_2(2m_N; m_\pi, m_\pi)\Phi_3(\sqrt{s}; m_\pi, m_\pi, m_\pi)}, \tag{33}$$

where $R_0 = 0.152$ is the ratio of the 2π and 3π final state probabilities for the $p\bar{p}$ annihilation at rest (see Table VI in Ref. [2]). For the zero total charge Q of the annihilating $\bar{p}N$ pair, the charge states of the outgoing pions were also determined from the data compilation of Ref. [2]. Since for $Q = \pm 1$ the data are absent, the charges of the 3π final states were determined by assuming that the $\pi^Q\pi^0\pi^0$ and $\pi^Q\pi^+\pi^-$ final channels have equal probabilities. The momenta of the outgoing pions were distributed microcanonically according to the available two- or three-body phase space.

After the annihilation is simulated, the residual nucleons and produced mesons were propagated in time according to the full kinetic equations (12), including both the baryonic mean fields and collision integrals. This takes into account the entropy production caused by the two-body collisions at the expansion stage. Moreover, important processes of the meson rescattering and absorption, e.g., $\pi N \to \Delta \to \pi N$ or $\pi N \to \Delta$, $\Delta N \to NN$ are included in the collision integral. These processes influence the observed particle spectra.

III. TIME EVOLUTION OF BOUND $\bar{p}$-NUCLEAR SYSTEMS

A. Initial compression stage

As demonstrated in Refs. [1,2] by static RMF calculations, a deeply-bound antiproton-nucleus system can be significantly compressed as compared with a normal nucleus. Now we want to study the real dynamics of such a system starting from the unperturbed nuclear ground state at $t = 0$.

Figure 3 (top panels) shows the nucleon and antiproton density profiles calculated at different times along the axis z drawn through the center of the $\bar{p}^{40}$Ca system. Figure 3 (bottom panels) also shows the nucleon and antiproton

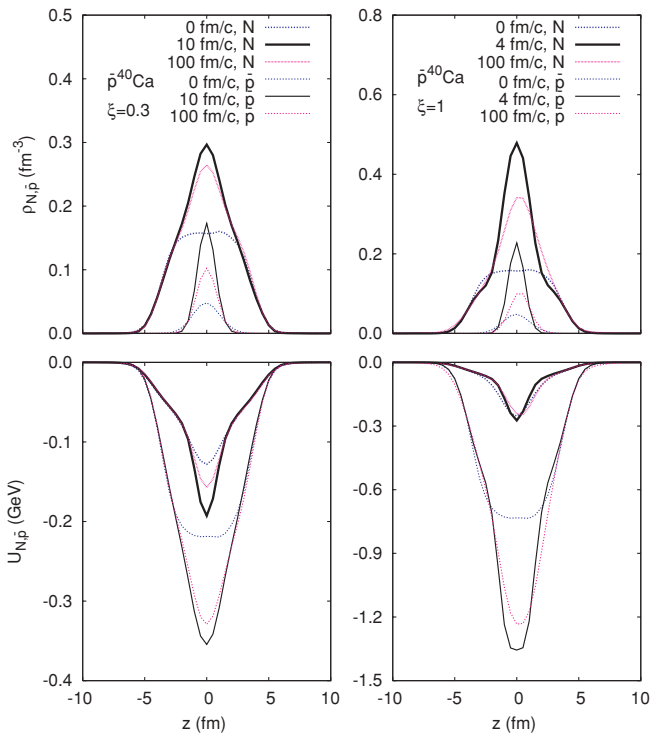

FIG. 3. (Color online) Nucleon and antiproton densities (top panels) and potentials (bottom panels) vs coordinate z on the axis passing through the center of the $\bar{p}^{40}$Ca system at selected times indicated in the figure. The calculations with the scaling factor $\xi = 0.3$ ($\xi = 1$) are shown in the left (right) panels. Please, notice different scales on vertical axis.

potentials $U_j \equiv g_{\omega j}\omega^0 + g_{\sigma j}\sigma$, $j = N, \bar{p}$, along the same axis. Left and right panels present results for $\xi = 0.3$ and $\xi = 1$, respectively. We see that the initial configuration is unstable and the system starts to shrink. Both nucleon and antiproton central densities grow quite fast, reaching their maxima within several fm/c. In the course of the compression process, the nucleon potential becomes deeper in the case of the reduced antiproton coupling constants ($\xi = 0.3$) and does not, practically, change in the G-parity motivated case ($\xi = 1$). The antiproton potential deepens quite strongly with time for the both sets of the antiproton coupling constants.

In the case of $\xi = 0.3$, the first maximum of the central nucleon density ($\rho_N = 0.30$ fm^{-3}) is reached at $t = 10$ fm/c. At later time the system rebounds and oscillates approaching gradually a static configuration with the nucleon density $\rho_N \simeq 0.26$ fm^{-3} at the center. Since the annihilation is switched off in this calculation, the compressed configuration may exist, in principle, infinitely long time. However, due to numerical reasons, the stability is destroyed by a gradual test particle escape from a box in the coordinate space, where the mean field is computed. Nevertheless, the numerical accuracy is good enough to trace the stable system up to at least $t = 100$ fm/c.

In the case of $\xi = 1$, the compression process is much faster than in the case of $\xi = 0.3$. Already at $t = 4$ fm/c we observe the first maximum of the central nucleon density with $\rho_N = 0.48$ fm^{-3}. A smaller value $\rho_N \simeq 0.34$ fm^{-3} is reached asymptotically after some oscillations.

In Fig. 4 we compare time evolution of the nucleon density distribution along the central axis z for the light ($\bar{p}^{16}$O) and heavy ($\bar{p}^{208}$Pb) systems. For $\bar{p}^{16}$O, the bell-like shape of the density distribution is reached quite fast. However, in the case of $\bar{p}^{208}$Pb, we observe a quickly growing peak in the center, while peripheral nucleons still do not react on the compression. This leads to the delayed shape equilibration via a complicated compression-decompression cycle.

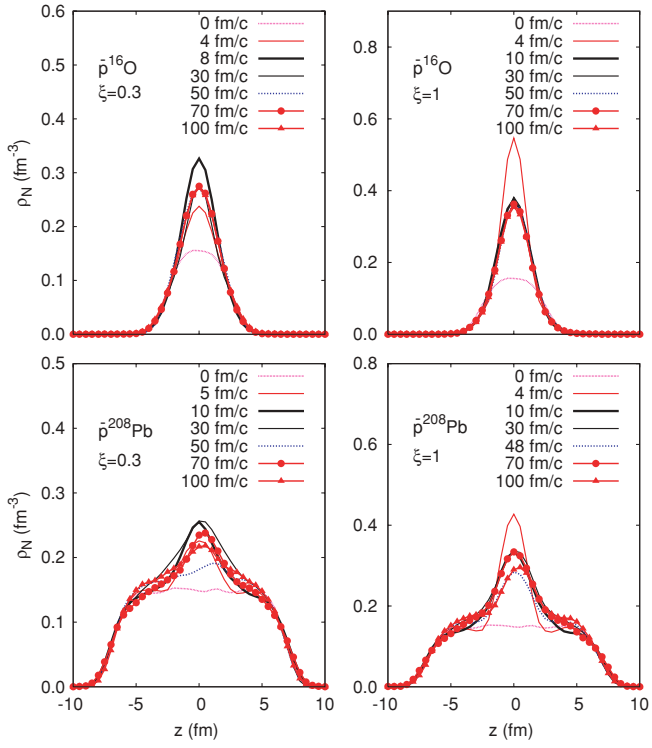

FIG. 4. (Color online) Nucleon densities along coordinate z at various time moments for $\bar{p}^{16}$O and $\bar{p}^{208}$Pb at $\xi = 0.3$ and $\xi = 1$.

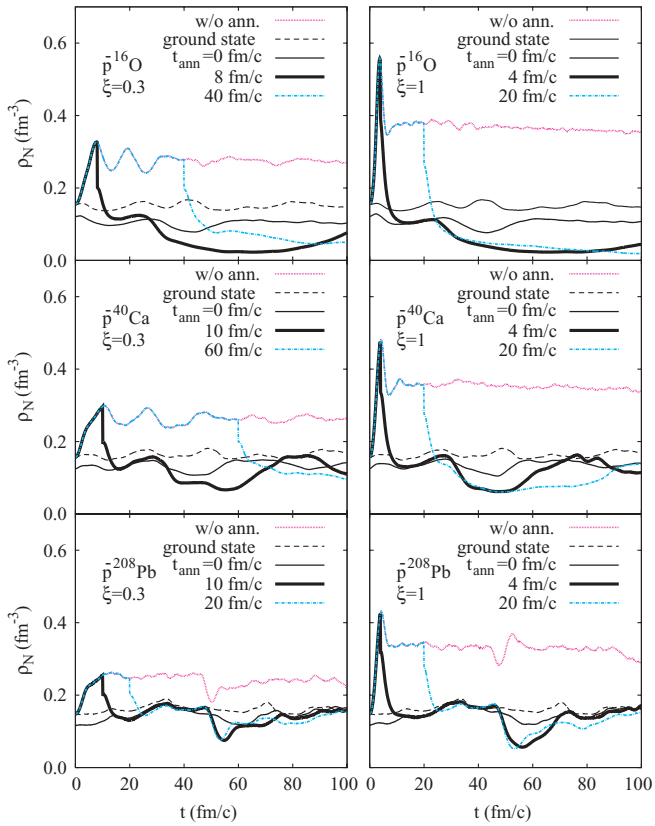

FIG. 5. (Color online) Time dependence of the nucleon density at the center of the $\bar{p}^{16}$O, $\bar{p}^{40}$Ca and $\bar{p}^{208}$Pb systems for two values of the scaling factor $\xi = 0.3$ (left panels) and $\xi = 1$ (right panels) of the antiproton coupling constants. The dotted line shows the calculation without $\bar{p}$ annihilation. The thin solid, thick solid and dash-dotted lines show the results with annihilation simulated at various times $t_{\rm ann}$ indicated in the figure. The dashed lines show the central nucleon density evolution for the corresponding ground state nucleus without an antiproton.

Figure 5 shows the time evolution of the central nucleon density for the three systems: $\bar{p}^{16}$O, $\bar{p}^{40}$Ca and $\bar{p}^{208}$Pb. The case without annihilation is shown by the dotted lines. For a comparison, we also present the central density time evolution in the respective ground state nuclei without an antiproton inside (dashed lines). We see, that at long enough times of the order of several tens fm/c, the static compressed configuration is indeed reached. The small oscillations of the central density in the compressed system visible at $t > 50$ fm/c are approximately of the same amplitude as the oscillations of the respective ground state. Thus, the reason for these small amplitude oscillations is the fermionic ground state instability due to the classical treatment of particles [26,36–39]. In principle, this instability can be removed by either employing the Pauli potential as in Refs. [36–38] or by adding a friction

force to the Hamiltonian equations of motions for the test particles [39]. Such modifications are beyond the scope of the present work. We expect that they would not essentially modify the density profiles of the compressed configurations, which are in an overall agreement with the previous static Hartree calculations of Refs. [1,2].

One can also notice (see lower panels of Fig. 5) a peculiar feature of the $\bar{p}^{208}$Pb system: the dip in the central nucleon density at $t \simeq 50$ fm/c. This is mostly a consequence of the delayed shape equilibration mentioned above in discussing Fig. 4. The especially strong density drop for $\xi = 0.3$ is partly caused by the symmetry loss due to the finite number of test particles. The dip is absent in lighter systems, since the shape equilibration for them is much faster (10–20 fm/c, see upper panels in Figs. 3 and 4).

Since the compression time is of primary importance, we have also studied the sensitivity of our results to the width σ_r of the initial antiproton DF (29). We have found, that for a larger (smaller) width the compression time becomes somewhat longer (shorter). In-particular, for the $\bar{p}^{16}$O system at $\xi = 1$ the time needed to reach the first density maximum is 5 fm/c (2.5 fm/c) for $\sigma_r = 2$ fm ($\sigma_r = 0.5$ fm). For the same system at $\xi = 0.3$ the first density maximum is reached at 10 fm/c (3 fm/c) for $\sigma_r = 2$ fm ($\sigma_r = 0.5$ fm). The value of the maximum density reached in the compression process is practically insensitive to σ_r.

We have to admit also, that there is some numerical uncertainty in our calculations due to the choice of the width L of the test particle Gaussian and the grid step size; e.g., in the calculation with $\Delta_x = \Delta_y = \Delta_z = L = 0.33$ fm for the lightest system $\bar{p}^{16}$O the maximum and saturation densities are 20% higher than in calculation with $\Delta_x = \Delta_y = \Delta_z = L = 0.5$ fm. Setting the smaller grid step is not feasible for technical reasons. Overall, this numerical uncertainty is comparable to the one due to different choices of the scaling factor ξ in our calculations.

B. Post-annihilation dynamics of residual nuclei

Next, we study the dynamics of a residual nucleus after sudden annihilation of an antiproton. The annihilation was simulated as described in Sec. II E. For each considered $\bar{p}A$ system and the scaling factor ξ, three different annihilation times $t_{\rm ann}$ have been chosen: They correspond to (i) the early ($t_{\rm ann} = 0$) annihilation from a noncompressed ground-state nucleus, (ii) the annihilation at the time moment when the first maximum of the central density is reached, and (iii) the late annihilation from an asymptotic compressed configuration.

One can see from Fig. 5, that the annihilation from a noncompressed ground state nucleus (thin solid lines) does not lead to significant expansion of the residual nuclear system. The central nucleon density stays always below but close to ρ_0 in this case. In the case of annihilation from the compressed configurations (thick solid and dash-dotted lines), we observe that, for the light systems $\bar{p}^{16}$O and $\bar{p}^{40}$Ca, the central nucleon density decreases sharply after annihilation and reaches values well below ρ_0. This is a clear indication of the collective expansion of a system from the initially compressed state. On the other hand, for the heavy $\bar{p}^{208}$Pb system, the expansion is not very pronounced at any choice of the annihilation time.

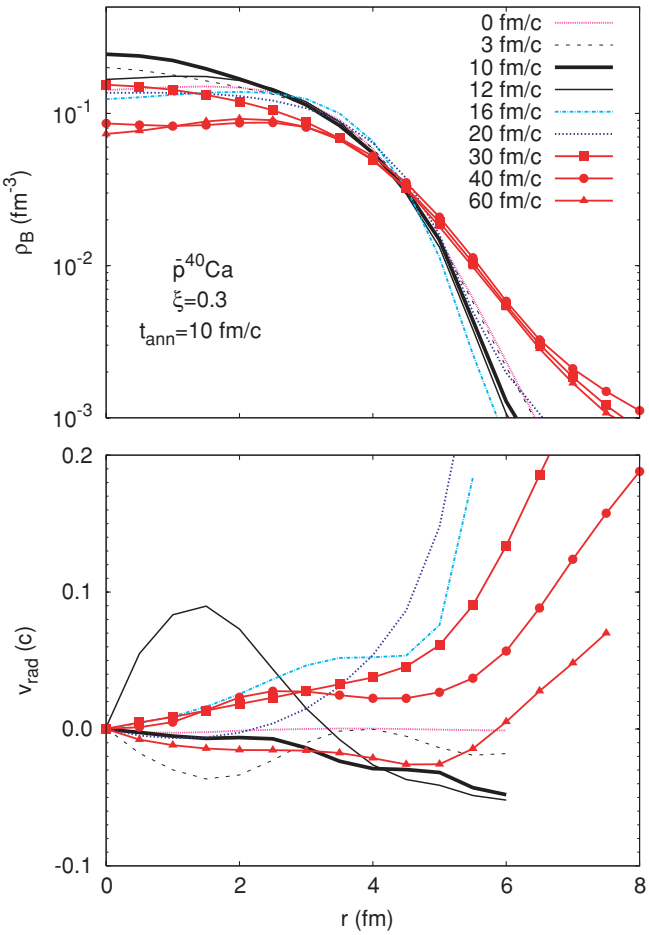

FIG. 6. (Color online) The baryon density (top panel) and the radial collective velocity (bottom panel) as functions of the radial distance for the $\bar{p}^{40}$Ca system computed with $\xi = 0.3$. The annihilation time $t_{\rm ann}$ was set to 10 fm/c.

It is interesting, that if the annihilation is switched on at the first density maximum (thick solid lines), then after an abrupt falling down the central density stays for some time ∼10–20 fm/c close to ρ_0 before decreasing further. This is explained by an inertial compression: After annihilation, the periphery of a residual nucleus still continues to move to the center during some time until rebound. In the case of the $\bar{p}^{40}$Ca system, this is demonstrated in Figs. 6 and 7, where we show the baryon density and the radial collective velocity,

$$v_{\rm rad} = \mathbf{r} \cdot \mathbf{v}_{\rm coll}/r, \tag{34}$$

at several times as a function of the radius r. The collective velocity has been determined as

$$v^{\alpha}_{\rm coll} = T^{\alpha 0}/T^{00}, \quad \alpha = 1, 2, 3. \tag{35}$$

At $r > 4$ fm, the evolution of the radial collective velocity field is noticeably influenced by the fermionic ground state instability discussed above. Nevertheless, one can still observe the inertial compression. Indeed, the radial collective velocity at $t = 12$ fm/c for $\xi = 0.3$ and at $t = 6$ fm/c for $\xi = 1$ reveals

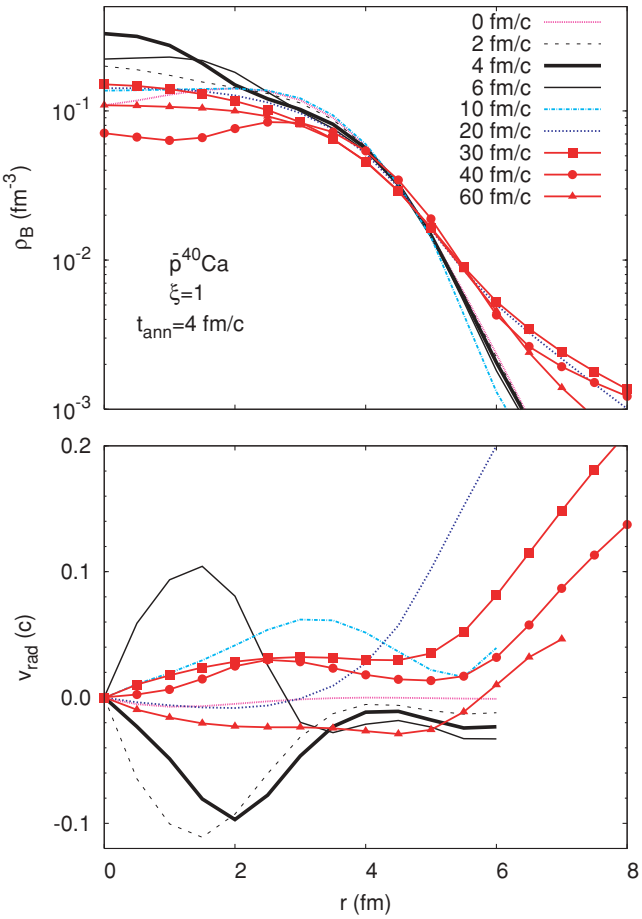

FIG. 7. (Color online) Same as in Fig. 6, but for $\xi = 1$ and $t_{\rm ann} = 4$ fm/c.

the fast outward motion at the center, while the peripheral nucleons still continue to move to the center. This explains plateaus in the central density evolution near $t \simeq 20$ fm/c in Fig. 5. At $t \simeq 30$ fm/c the whole system starts to expand. This is reflected in the monotonically increasing radial collective velocity with radius. The especially strong rise of $v_{\rm rad}$ at large r is due to emission of fast particles. At later times $t \simeq 50$–60 fm/c the expansion is replaced by the inward motion of the matter in the central zone. However, the fast particles are still continuing to escape from the dense region. We expect that in reality the system will break-up into fragments before the inward motion will start (see discussion Sec. IV A).

IV. OBSERVABLE SIGNALS

A. Multifragmentation of residual nuclei

It is presently well established (see [40] and references therein) that nuclear matter at low densities ($\rho < 0.6\,\rho_0$) becomes unstable with respect to small density perturbations, so called spinodal instability. However, in order these density perturbations to develop into nuclear fragments, the system must stay long enough time ~30 fm/c in the spinodal region. One can see from Fig. 5, that the light systems $\bar{p}^{16}$O and $\bar{p}^{40}$Ca spend a long time in this region. Therefore, the residual nuclear systems can undergo a multifragment breakup, if the annihilation happens in the compressed configurations. In other words, the multifragment breakup of nuclei after the $\bar{p}$-annihilation may serve as a signal of the compression prior the annihilation.

In Table I we collect the estimated parameters of fragmenting sources for the $\bar{p}^{16}$O and $\bar{p}^{40}$Ca systems. The case of $\bar{p}$-annihilation from the state of maximum central density is considered here (see thick solid lines in Fig. 5). The sources have been determined by selecting nucleons in the space region where the baryon density is larger than $\rho_{\rm min} = 0.01\rho_0$. They are characterized by the neutron (N) and proton (Z) numbers, the collective kinetic energy per nucleon ($E^{\rm coll}_{\rm kin}$) and the residual excitation energy per nucleon ($E^{\star}_{\rm res}$). These parameters are defined as

$$N = \int\limits_{\rho>\rho_{\rm min}} d^3r\rho_n(\mathbf{r}), \quad Z = \int\limits_{\rho>\rho_{\rm min}} d^3r\rho_p(\mathbf{r}), \tag{36}$$

$$E^{\rm coll}_{\rm kin} = \frac{1}{A}\int\limits_{\rho>\rho_{\rm min}} d^3r\left(T^{00} - \sqrt{T^{\mu 0}T^0_\mu}\right), \tag{37}$$

$$E^{\star}_{\rm res} = \frac{1}{A}\int\limits_{\rho>\rho_{\rm min}} d^3rT^{00} - E_{\rm g.s.}(N,Z) - E^{\rm coll}_{\rm kin}, \tag{38}$$

where ρ_n and ρ_p are the neutron and proton densities, respectively; $A = N + Z$; and $E_{\rm g.s.}(N, Z)$ is the ground state energy per nucleon of a nucleus with neutron number N and proton number Z computed within our model. The collective

TABLE I. Fragmenting source parameters for the different annihilating systems and values of the scaling factor ξ of the antiproton coupling constant. $t_{\rm ann}$ denotes the annihilation time moment. t is the time moment when the source parameters have been determined. ρ_N is the central nucleon density. Z, $E^{\rm coll}_{\rm kin}$ and $E^{\star}_{\rm res}$ are the charge number, collective kinetic energy per nucleon and residual excitation energy per nucleon, respectively (see Eqs. (36), (37) and (38)).

System	ξ	$t_{\rm ann}$ (fm/c)	t (fm/c)[a]	ρ_N (fm^{-3})	Z[a]	$E^{\rm coll}_{\rm kin}$ (MeV/nucleon)	$E^{\star}_{\rm res}$ (MeV/nucleon)
$\bar{p}^{40}$Ca	0.3	10	40	0.086	17	0.6	8.1
$\bar{p}^{40}$Ca	1.0	4	40	0.071	16	0.3	6.3
$\bar{p}^{16}$O	0.3	8	35	0.057	6	2.0	9.9
$\bar{p}^{16}$O‡	0.3	8	35	0.056	6	2.1	9.6
$\bar{p}^{16}$O	1.0	4	36	0.051	5	1.4	7.9
$\bar{p}^{16}$O‡	1.0	4	36	0.051	5	1.5	7.8

[a]Including Coulomb interaction in propagation of the test particles.

kinetic energy (37) is calculated neglecting pressure effects. Due to the initially isospin-symmetric nuclei and the neglect of the isovector mesons in the Lagrangian density (3), we obtained in all cases $N \simeq Z$ in the source. It turned out also, that the Coulomb interaction optionally included in some of the calculations does not change this result. Thus, only the charge numbers Z are given in Table I. The time moment for determination of the source parameters has been chosen at 35–40 fm/c, when the central nucleon density is about 1/3–1/2ρ_0, i.e., inside the spinodal region. The calculated residual excitation energy is typically 6–10 MeV/nucleon that corresponds to the temperatures 4–7 MeV. According to the statistical multifragmentation model [41], in this energy domain the multifragment breakup is the dominating decay channel of residual nuclei. The collective kinetic energy is 1.4–2.1 MeV/nucleon in the case of $\bar{p}^{16}$O. This is well above the Coulomb energy of the source, which is only about 0.4 MeV/nucleon for $N = Z = 5$. Unfortunately, such a source is too small to experience the real multifragment breakup, rather a Fermi breakup into small clusters [41]. In the case of larger sources, produced in $\bar{p}^{40}$Ca annihilation the collective kinetic energy is considerably smaller, 0.3–0.6 MeV/nucleon, but still significant with respect to the total Coulomb energy $\simeq$1.0 MeV/nucleon for $N = Z = 16$. Thus, we expect some signs of collective expansion to be visible in kinetic energy spectra of produced fragments.

B. Knock-out nucleon spectra

Let us now consider other observable effects. Figure 8 shows the c.m. kinetic energy spectra of the nucleons emitted from the $\bar{p}^{16}$O, $\bar{p}^{40}$Ca, and $\bar{p}^{208}$Pb systems after the $\bar{p}$-annihilation. In order to separate emitted nucleons from the bound nucleons of a residual nucleus, we used a simple criterion: only those nucleons, both protons and neutrons, were included in the spectra which are separated by at least 3 fm from the other test particles of a given parallel ensemble at $t = 100$ fm/c. One can see, that nucleons with the kinetic energy $E_{\rm kin} \gg E_{\rm F}$, where $E_{\rm F} \simeq 35$ MeV is the Fermi energy of the nuclear matter at ρ_0, are abundantly emitted. Such nucleons are knocked-out from the nucleus by the mesons produced after the annihilation [14].

In Table II we list the slope parameters T_N of the nucleon kinetic energy spectra obtained by the Maxwell-Boltzmann fit

$$\frac{dN_{\rm nuc}}{dE_{\rm kin}} \propto \sqrt{E_{\rm kin}}\exp(-E_{\rm kin}/T_N) \qquad (39)$$

in the region of $E_{\rm kin} = 200$–500 MeV. We would like to mention, that the authors of Ref. [14] report the slope temperature of about 60 MeV for the kinetic energy spectrum of the emitted protons in the case of $\bar{p}^{40}$Ca system, which is not so far from our results for the annihilation in the ground-state nucleus at $t_{\rm ann} = 0$.

We want to emphasize that the kinetic energy spectra of nucleons emitted after the $\bar{p}$-annihilation from the compressed $\bar{p}^{16}$O, and $\bar{p}^{40}$Ca systems are significantly harder than the spectra of nucleons from the annihilation at $t_{\rm ann} = 0$. This can be explained by two effects. First, the collective expansion of the outer shell will increase the slope temperature, typically, by several MeV (see Table I and Figs. 6, 7). Second, just after the annihilation the nucleon potential at the center of a nucleus grows suddenly by ~80–300 MeV. This creates an additional push for the fast nucleons emitted from the nucleus. Although the hardening effect is most pronounced for the lightest system $\bar{p}^{16}$O, it is also quite visible for $\bar{p}^{40}$Ca. For the heaviest system $\bar{p}^{208}$Pb, we observe almost identical high energy tails of the nucleon spectra for the different annihilation times. The reason is that the collective expansion is practically absent in this system (see Fig. 5). Also, the yield of fast nucleons is reduced by their subsequent rescatterings in the residual nucleus.

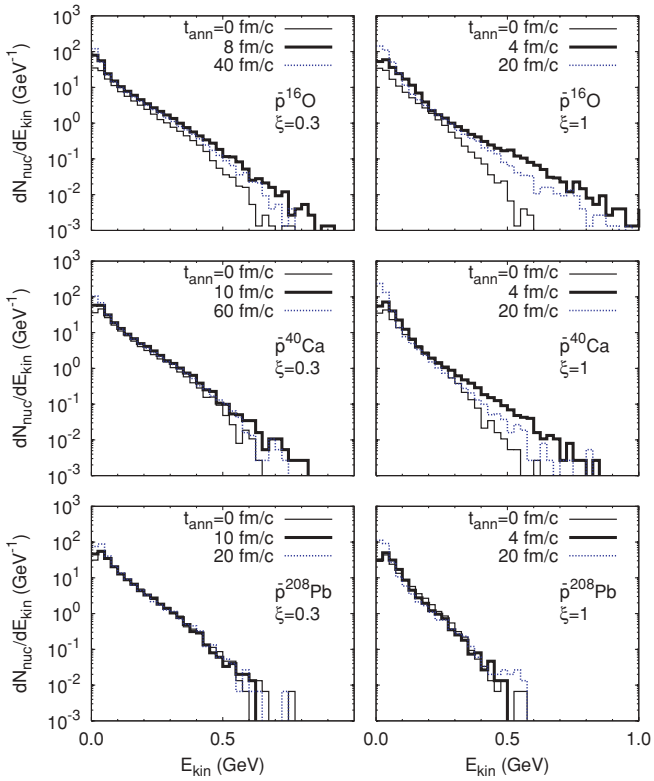

FIG. 8. (Color online) Kinetic energy spectra of emitted nucleons in the c.m. frame for various $\bar{p}$A systems and values of the parameter ξ. Different histograms correspond to different values of the annihilation time $t_{\rm ann}$ indicated in the key.

TABLE II. Slope temperatures T_N (MeV) for the nucleon kinetic energy spectra (see Fig. 8 and Eq. (39)). Only the values of T_N for $t_{\rm ann} = 0$ (first number) and for the annihilation at the time of the maximum compression (second number) are given. Statistical error is ±2 MeV.

ξ	$\bar{p}^{16}$O	$\bar{p}^{40}$Ca	$\bar{p}^{208}$Pb
0.3	66, 81	67, 71	64, 59
1	52, 95	46, 79	45, 53

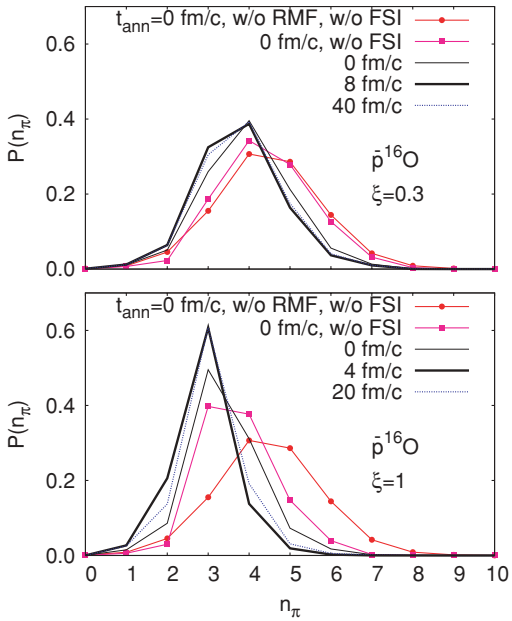

FIG. 9. (Color online) Pion multiplicity distributions for the $\bar{p}^{16}$O system. The line with full circles shows the calculation without mean field and without FSI after the annihilation. The line with full boxes shows the result with mean field, but without FSI. Other lines show the full calculation at various choices of the annihilation time (shown in the key). The top (bottom) panel presents results for $\xi = 0.3$ ($\xi = 1$).

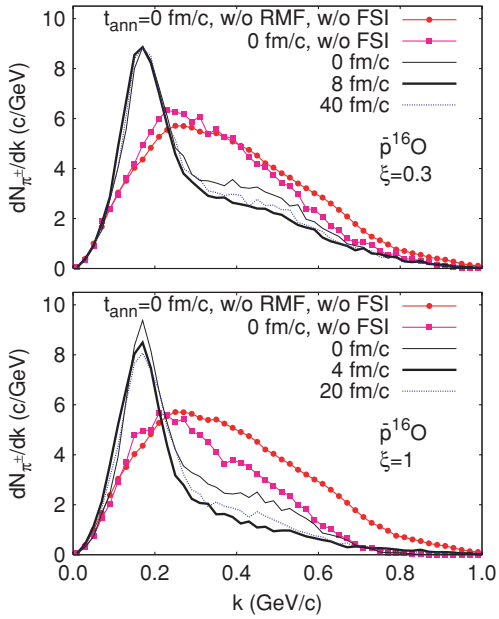

FIG. 10. (Color online) Same as in Fig. 9, but for the charged pion momentum distributions in the c.m. frame of the $\bar{p}^{16}$O system.

C. Mesonic observables

The meson production from the $\bar{p}$-annihilation inside nucleus is influenced both by the mean field via the potentials of the annihilating pair and by the final state interactions (FSI), i.e., the two-body collisions and resonance decays. It is instructive to disentangle the contributions of the mean field effects from the rescattering and absorption effects. To this aim, we have performed additional calculations by subsequently switching off the FSI and the mean field. Corresponding results are shown in Figs. 9, 10 and 11.

Figure 9 shows pion multiplicity distributions for the $\bar{p}^{16}$O system. In the case of reduced antiproton coupling constants ($\xi = 0.3$), the mean field alone does not produce any noticeable modification of the pion multiplicity distribution. On the other hand, FSI leads to a rather substantial shift toward smaller n_π. For the case of $\xi = 1$, we observe a strong pion multiplicity reduction due to smaller $\sqrt{s}$ for the $\bar{p}N$ annihilation, while the FSI effects are much weaker. One can also see a quite significant compressional effect for $\xi = 1$, which is only very weak for $\xi = 0.3$.

In Fig. 10, we present charged pion momentum spectra in the c.m. frame of the $\bar{p}^{16}$O system. FSI strongly modifies these spectra, mostly due to the $\pi N \to \Delta \to \pi N$ processes, which effectively decelerate pions. As we have already observed earlier in Fig. 8, emitted nucleons gain energy, correspondingly.

The effect of the baryonic mean field on the pion momentum spectrum is relatively moderate: we observe some depletion of the high-momentum tail, which is more pronounced in the case of $\xi = 1$. The compressional effect is visible in the reduction of the pion yield in the momentum range $0.3 \leqslant k \leqslant 0.6$ GeV/c. This can be understood from Figs. 2 and 9: in vacuum, the events with $n_\pi = 5$ and $n_\pi = 6$ contribute substantially to this momentum range, while the probability of such events

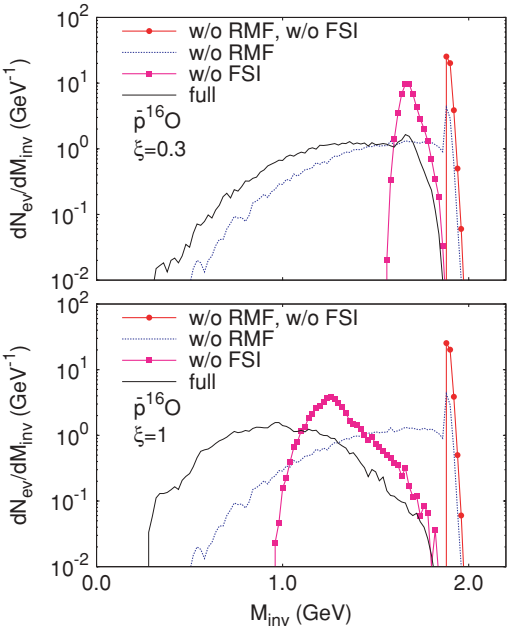

FIG. 11. (Color online) Distribution of the annihilation events on the total invariant mass of emitted mesons for the $\bar{p}^{16}$O system. The calculation without mean field and without FSI is shown by the line with full circles. The results without mean field but with FSI are shown by the dotted line. The line with full boxes shows the result with mean field, but without FSI. The full calculation is presented by the solid line. Upper (lower) panel corresponds to $\xi = 0.3$ ($\xi = 1$). Only calculations at $t_{\rm ann} = 0$ are shown.

is substantially suppressed in a compressed nucleus due to the reduced annihilation phase space [2].

The pion momentum spectrum has clearly the two components: the slow pions, which have undergone rescatterings via the Δ-resonance excitation (k less than about 300 MeV/c), and the high energy pions, which were emitted from the system almost without secondary interactions. The similar result has been obtained in earlier intranuclear cascade calculations [14]. Following Ref. [14], we have also fitted the low energy part of the pion spectrum ($E - m_\pi = 100$–150 MeV, $E = \sqrt{k^2 + m_\pi^2}$) by the Maxwell-Boltzmann distribution

$$\frac{dN_{\pi^\pm}}{dk} = k^2 \exp(-E/T_\pi). \tag{40}$$

This fit has produced the following slope temperatures of the charged pion momentum spectrum for the $\bar{p}^{16}$O system: $T_\pi \simeq 45$ MeV and 44 MeV for $\xi = 0.3$ ($T_\pi \simeq 43$ MeV and 36 MeV for $\xi = 1$) in the case of early annihilation ($t_{\rm ann} = 0$) and annihilation at the time of maximum compression, respectively. The extracted T_π is smaller than the slope temperature of 53 MeV of the low energy pions for the $\bar{p}^{40}$Ca system reported in Ref. [14]. However, in the calculation without mean field, we obtain $T_\pi \simeq 51$ MeV, which is in a good agreement with the result of Ref. [14]. Therefore, the difference between our results and those of Ref. [14] is caused by the mean field acting on the annihilating pair in medium. Moreover, we see the softening of the pion spectrum in the case of larger antinucleon couplings due to smaller $\sqrt{s}$ of the annihilating pair.

Figure 11 presents the distributions of the annihilation events in the total invariant mass of produced mesons from the $\bar{p}^{16}$O system. The invariant mass is defined as

$$M_{\rm inv} = \left(\left(\mathrm{P}^0_{\rm mes}\right)^2 - \mathbf{P}^2_{\rm mes}\right)^{1/2}, \tag{41}$$

where $\mathrm{P}^\mu_{\rm mes} = \sum_i p_i^\mu$ is the sum of four-momenta of the mesons produced in a given annihilation event. The calculations were done for the case of $t_{\rm ann} = 0$.

In the absence of FSI, $M_{\rm inv}$ should be equal to the invariant energy $\sqrt{s}$ of the annihilating $\bar{p}N$ pair. Indeed, without FSI and without mean field, as expected, we get a quite sharp peak at $2m_N$ only slightly smeared out due to the Fermi motion of nucleons and momentum spread of the initial antiproton DF (29). The baryonic mean field leads to the shift of a peak position toward smaller $M_{\rm inv}$ and to some broadening of the distribution. The broadening is due to the spatial spread of the initial antiproton DF (29), which results in different mean-field potentials acting on different annihilating $\bar{p}N$ test particle pairs. Additionally, the FSI leads to a very strong broadening of the invariant mass spectrum due to the deceleration and absorption of the annihilation mesons. This is clearly seen in Fig. 11 for the case when the RMF was switched off (dotted line). Nevertheless, the full calculation (solid line) shows quite strong softening of the $M_{\rm inv}$ distribution due to the mean-field effects. Obviously, this effect is stronger for the case of $\xi = 1$ as compared with $\xi = 0.3$.

Finally, in Fig. 12, we systematically study how the meson invariant mass spectra are affected by the nuclear compression effects. The results are shown for the different $\bar{p}$-nucleus systems. Due to the strong reduction of the nucleon

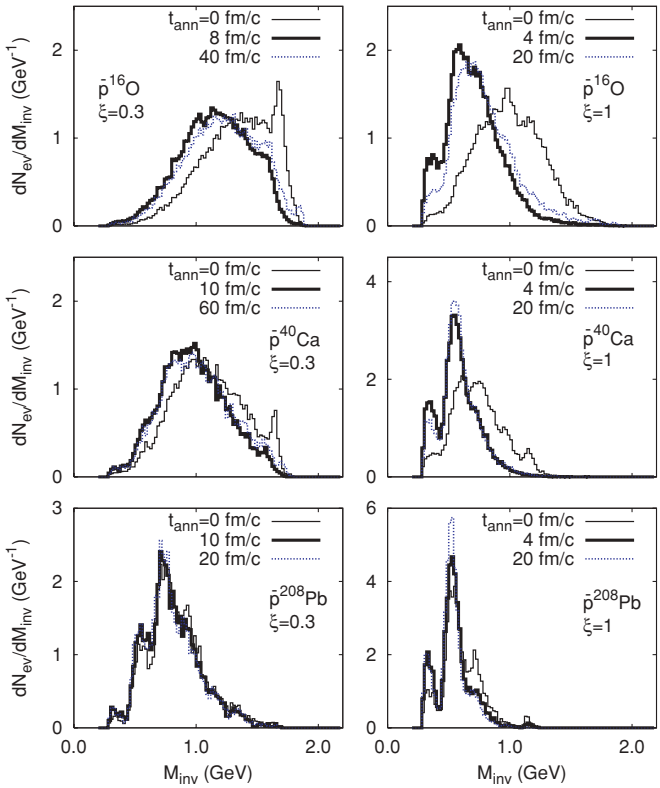

FIG. 12. (Color online) Annihilation event distributions on the total invariant mass of emitted mesons for various $\bar{p}$A systems and values of the parameter ξ. Different histograms correspond to different values of the annihilation time $t_{\rm ann}$ indicated in the key.

effective mass with the scalar density, the meson invariant mass spectra become softer when the annihilation happens in the compressed configurations, as compared with the annihilation in the normal state at $t_{\rm ann} = 0$. The effect is, again, more pronounced for the light systems $\bar{p}^{16}$O and $\bar{p}^{40}$Ca. In the $\bar{p}^{16}$O system the shift is almost 500 MeV even in the case of $\xi = 0.3$.

We believe that results presented in Figs. 8, 9, 10, and 12 constitute the set of observables sensitive to the compressional effects in nuclei induced by an antiproton.

V. SUMMARY AND OUTLOOK

We have performed dynamical modeling of possible compression effects in nuclei due to the presence of an antiproton. The semiclassical transport GiBUU model [10] incorporating the relativistic mean fields for the baryons and antibaryons has been employed in calculations. The model reproduces reasonably well the earlier static calculations of bound $\bar{p}$-nuclear systems [1,2].

In this work, we did not consider the stopping process of an incident antiproton in a target nucleus. This is a rather complicated problem due to the unknown in-medium cross sections of the $\bar{p}$-scattering and annihilation. This problem will be addressed in a forthcoming paper. Instead, we have assumed, that the antiproton has penetrated to the center of the nucleus, stopped there due to an inelastic collision, and then get captured to the lowest energy state. Such events should be

very rare, with a probability of the order of 10^{-4} for the central collisions [2]. As proposed in Ref. [2], formation of bound antiproton-nucleus states can be triggered by the emission of fast nucleons, pions or kaons. We have shown, that during the time interval of 4–10 fm/c after creation of the initial state the central density of the target nucleus grows up to the values of 2–3ρ_0 depending on somewhat uncertain values of the antiproton coupling constants. We expect that the life time of strongly bound antiprotons can be long enough to observe this cold compression effect.

Detailed kinetic simulations of the post-annihilation evolution of residual nuclei have been carried out at different assumptions on the annihilation time. It is shown, that the $\bar{p}$-annihilation in compressed light systems, like $\bar{p}^{16}$O and $\bar{p}^{40}$Ca, leads to the pronounced collective expansion of the residual nucleus, which may result in the multifragment breakup. Another clear signature of the nuclear compression is the hardening of the kinetic energy spectra of emitted nucleons. On the other hand, the invariant mass distribution of produced mesons is shifted to smaller invariant masses due to the in-medium reduction of the nucleon effective mass at high scalar density. Similar phenomena are expected also for the case of $\bar{\Lambda}$-nucleus bound states which can be produced via the $\bar{p}p \to \bar{\Lambda}\Lambda$ reaction on nuclei.

Another interesting possibility is that the compressed zone of the nucleus might undergo a deconfinement phase transition. Then one can expect formation of a quark-antiquark droplet with a nonzero baryon number and relatively low temperature [2].

Our main assumption in the present study was that the annihilation takes place in the central region of a nucleus. The experimental selection of the central annihilation events is a difficult problem. No clear trigger condition for such events has been invented so far. One suggestion is that the central annihilation events, in average, will be characterised by isotropic emission of secondary particles and high fragment multiplicity [13,14]. However, further theoretical and experimental efforts are needed to develop a good trigger condition for the central annihilation. Despite of these difficulties, we propose to study the above predictions in antiproton-nucleus reactions at the future Facility for Antiproton and Ion Research (FAIR) at GSI (Darmstadt).

ACKNOWLEDGMENTS

The support by the Frankfurt Center for Scientific Computing is gratefully acknowledged. The authors are grateful to A. S. Botvina, Th. J. Bürvenich, I. A. Pshenichnov, J. Ritman, and H. Stöcker for stimulating discussions. This work has been partially supported by DFG Grant No. 436 RUS 113/711/0-2 (Germany) and Grant No. NS-3004.2008.2 (Russia).

[1] T. Bürvenich, I. N. Mishustin, L. M. Satarov, J. A. Maruhn, H. Stöcker, and W. Greiner, Phys. Lett. **B542**, 261 (2002).
[2] I. N. Mishustin, L. M. Satarov, T. J. Bürvenich, H. Stöcker, and W. Greiner, Phys. Rev. C **71**, 035201 (2005).
[3] W. Greiner and B. Müller, *Quantum Mechanics: Symmetries* (Springer-Verlag, Berlin/Vienna/New York, 2001).
[4] C.-Y. Wong, A. K. Kerman, G. R. Satchler, and A. D. MacKellar, Phys. Rev. C **29**, 574 (1984).
[5] S. Teis, W. Cassing, T. Maruyama, and U. Mosel, Phys. Rev. C **50**, 388 (1994).
[6] C. J. Batty, E. Friedman, and A. Gal, Phys. Rep. **287**, 385 (1997).
[7] E. Friedman, A. Gal, and J. Mareš, Nucl. Phys. **A761**, 283 (2005).
[8] E. Friedman and A. Gal, Phys. Rep. **452**, 89 (2007).
[9] C. B. Dover, T. Gutsche, M. Maruyama, and A. Faessler, Prog. Part. Nucl. Phys. **29**, 87 (1992).
[10] http://gibuu.physik.uni-giessen.de/GiBUU
[11] A. B. Larionov, O. Buss, K. Gallmeister, and U. Mosel, Phys. Rev. C **76**, 044909 (2007).
[12] C.-Y. Wong, Phys. Rev. C **25**, 1460 (1982).
[13] J. Rafelski, Phys. Lett. **B91**, 281 (1980).
[14] M. Cahay, J. Cugnon, P. Jasselette, and J. Vandermeulen, Phys. Lett. **B115**, 7 (1982).
[15] G. A. Lalazissis, J. König, and P. Ring, Phys. Rev. C **55**, 540 (1997).
[16] J. Boguta and A. R. Bodmer, Nucl. Phys. **A292**, 413 (1977).
[17] J. D. Walecka, Ann. Phys. (NY) **83**, 491 (1974).
[18] D. Vasak, M. Gyulassy, and H.-Th. Elze, Ann. Phys. (NY) **173**, 462 (1987).
[19] H.-Th. Elze, M. Gyulassy, D. Vasak, H. Heinz, H. Stöcker, and W. Greiner, Mod. Phys. Lett. A **A2**, 451 (1987).
[20] Yu. B. Ivanov, Nucl. Phys. **A474**, 669 (1987).
[21] B. Blättel, V. Koch, and U. Mosel, Rep. Prog. Phys. **56**, 1 (1993).
[22] K. Weber, B. Blättel, W. Cassing, H.-C. Dönges, V. Koch, A. Lang, and U. Mosel, Nucl. Phys. **A539**, 713 (1992).
[23] C. M. Ko, Q. Li, and R. Wang, Phys. Rev. Lett. **59**, 1084 (1987).
[24] R.S. Varga, *Matrix Iterative Analysis* (Prentice Hall, New Jersey, 1962).
[25] J. Aichelin, Phys. Rep. **202**, 233 (1991).
[26] J. P. Bondorf, O. Friedrichsen, D. Idier, and I. N. Mishustin, Nucl. Phys. **A624**, 706 (1997).
[27] G. Q. Li and R. Machleidt, Phys. Rev. C **48**, 1702 (1993).
[28] J. Cugnon, D. L'Hôte, and J. Vandermeulen, Nucl. Instrum. Methods Phys. Res. B **111**, 215 (1996).
[29] J. Geiss, W. Cassing, and C. Greiner, Nucl. Phys. **A644**, 107 (1998).
[30] J. Geiss, Ph.D. thesis, University of Giessen, 1998, http://theorie.physik.uni-giessen.de/html/dissertations.html.
[31] B. Andersson, G. Gustafson, G. Ingelman, and T. Sjöstrand, Phys. Rep. **97**, 31 (1983).
[32] J. Vandermeulen, Z. Phys. C **37**, 563 (1988).
[33] S. Mundigl, M. Vicente Vacas, and W. Weise, Nucl. Phys. **A523**, 499 (1991).
[34] J. Sedlák and V. Ŝimák, Fiz. Elem. Chastits At. Yadra **19**, 445 (1988); [Sov. J. Part. Nuclei **19**, 191 (1988)].
[35] M. Wagner, A. B. Larionov, and U. Mosel, Phys. Rev. C **71**, 034910 (2005).

[36] L. Wilets, E. M. Henley, M. Kraft, and A. D. Mackellar, Nucl. Phys. **A282**, 341 (1977).
[37] C. Dorso, S. Duarte, and J. Randrup, Phys. Lett. **B188**, 287 (1987).
[38] G. Peilert, J. Randrup, H. Stöcker, and W. Greiner, Phys. Lett. **B260**, 271 (1991).
[39] A. Bonasera, T. Maruyama, M. Papa, and S. Chiba, arXiv:nucl-th/0110068.
[40] Ph. Chomaz, M. Colonna, and J. Randrup, Phys. Rep. **389**, 263 (2004).
[41] J. P. Bondorf, A. S. Botvina, A. S. Iljinov, I. N. Mishustin, and K. Sneppen, Phys. Rep. **257**, 133 (1995).